Unveiling the nanostructured nature of pyrobitumen and shungite carbons through Raman, X-ray and theoretical analyses

Eric Faulques, Nataliya Kalashnyk, Yves Lulzac, Yves Moëlo

Carbon Trends 17 (2024) 100421

Contents lists available at ScienceDirect

Carbon Trends

journal homepage: www.elsevier.com/locate/cartre

Unveiling the nanostructured nature of pyrobitumen and shungite carbons through Raman, X-ray and theoretical analyses

Eric Faulques [a,*], Nataliya Kalashnyk [a], Yves Lulzac [b], Yves Moëlo [c]

[a] University Lille, CNRS, Centrale Lille, University Polytechnique Hauts-de-France, Junia-ISEN, UMR8520—IEMN, F-59000 Lille, France
[b] Centre de Recherche Gemmologique, 2 rue de la Houssinière, F-44322 Nantes cedex 3, France
[c] Nantes Université, CNRS, Institut des Matériaux de Nantes Jean Rouxel, IMN, F-44000 Nantes, France

ARTICLE INFO

Keywords:
Pyrobitumen ol Lopérec (France)
Shungite of Karelia
Graphitic carbon
Nanostructure
X-ray diffraction
Raman scattering
DFT

ABSTRACT

X-ray powder diffraction and multi-wavelength Raman spectroscopy were employed to characterize carbonaceous geomaterials, offering the first nanostructural analysis of rare pyrobitumen (LP) samples from the Lopérec gold deposit in Brittany, France, by comparing them to Karelian shungite (KS) and carbon allotropes samples. The inter-reticular distances $d_{(002)}$ for LP/KS, derived from X-ray diffraction patterns, are 3.57(1)/3.48(1) Å, with crystal thickness $Lc_{(002)}$ and graphitization degree of 1.4/2.0 nm and 6.9/13.1, respectively. Raman band deconvolution indicates graphitic domain sizes of L_a = 6.7/8.2 nm and graphene-like flake tortuosity L_t = 9.2/11.3 nm. Extensive density functional theory calculations on various 2D nanoflakes accurately predict that the D and G Raman bands may originate from graphene quantum dots, which form part of the nanostructure of these geomaterials. LP exhibits greater structural disorder than KS, along with a lower density (1.60 vs. 1.85 g/cm^3), suggesting a lower degree of graphitization, likely due to formation at a lower temperature (~300 °C). The Lopérec pyrobitumen is believed to result from a redox process involving a CO_2-rich, oxidizing hydrothermal solution interacting with a local hydrocarbon source.

1. Introduction

In nature, the evolution of carbon-based organic matter from diagenesis to strong metamorphism conditions can result in the formation of graphite, or to disordered material with carbon-rich composition (> 90 wt.%), such as anthracite and pyrobitumen (also known as anthraxolite). Pyrobitumen is generally considered as the ultimate residual solid end-product of organic matter in thermally mature oil reservoirs [1]. On a large scale, this geomaterial is a non-graphitizable, non-crystalline carbon that, even at high temperatures, does not convert to highly ordered graphite and instead keeps its amorphous structure composed of disordered sp^2 type carbon species. Another distinctive type of pyrobitumen [2,3] is shungite that forms giant deposits in Lower Proterozoic strata of Karelia (Russia), and whose genesis remains debated [4].

During ore prospecting in the Armorican Massif (western France) by the French geological survey (BRGM), an auriferous quartz-vein deposit was discovered in Lopérec, in the central Finistère department [5,6]. A mineralogical study of this deposit [7] revealed a significant presence of pyrobitumen.

The geology of Lopérec deposit located on the NW margin of the Châteaulin carboniferous basin, overlying Ordovician and Devonian formations (Fig. 1), has been presented by Bouchot et al. [5] and Marcoux [6]. It is subordinated to a NE-SW shearing within the Kermerrien formation of Strunian and Visean ages, composed of black shales, schists and quartzites. The tectonic process permitted the formation of mineralized quartz veins, as well as massive chert (silicified Strunian).

Four stages of ore deposition have been distinguished during the hydrothermal process. Main ore sulfides are pyrite (major), arsenopyrite and pyrrhotite, in a matrix of quartz and minor siderite [7]. Gold is subordinated to stage 1, and the end of stage 4. Organic matter was deposited in quartz-siderite veins and chert during stage 4. Pyrobitumen is well developed within this chert (up to ~10 % volume).

The microstructure of carbonaceous geomaterials is of significant interest due to their abundance as natural carbon resources and their potential applications in energy storage, functional carbon-based materials, and advanced composites. For instance, shungite has industrial potential in oxidation–reduction processes, water purification, and as an additive in diverse materials [8]. The nanostructure of shungite with graphene flakes, quantum dots, and other carbon species, presents

* Corresponding author.
E-mail address: eric.faulques@univ-lille.fr (E. Faulques).

https://doi.org/10.1016/j.cartre.2024.100421
Received 29 October 2024; Accepted 30 October 2024
Available online 9 November 2024

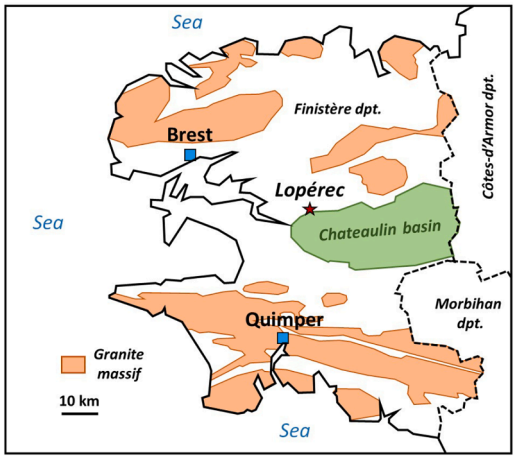

Fig. 1. Localization of Lopérec gold deposit (Finistère department, Brittany).

exciting opportunities for advanced applications in fields that harness the unique properties of nanosized carbon components as e.g. energy storage, composites, or absorption. Likewise, pyrobitumens—characterized by extensive and high-purity carbon reserves—should hold significant promise for similar applications.

In this study, an unprecedented in-depth analysis of the nanostructure of Lopérec pyrobitumen (LP) is conducted using a combination of X-ray diffraction (XRD), Raman spectroscopy, and density functional theory (DFT) calculations. The analytical results are compared with those obtained from a typical massive Karelian shungite (KS) sample, used as a reference. The implications for the graphitic nanostructures of the two specimens are discussed. Based on these analyses, the geoformation processes responsible for the natural development of Lopérec pyrobitumen are explored, and new hypotheses regarding its origin are proposed.

2. Experimental

Various pyrobitumen-rich samples were selected on ore dumps, where it forms millimetric- to centimetric-size aggregates, in white quartz and minor siderite. Inclusions of pyrite can be present in some samples.

The Hanneman balance [9] was used to measure the pyrobitumen density on minute pure fragments selected under the binocular. It yielded a density d of 1.60, compared to 1.85 for the shungite sample. This value is in agreement with the density variation of disordered sp^2 carbon (1.5–2.2) [10]. Mohs hardness (~ 6) is identical to that of the shungite sample. The metallic character of Lopérec carbonaceous matter was confirmed with a multimeter, while a diamond tester revealed poor thermal conductivity. These properties are typical of pyrobitumen, similar to shungite. Chemical composition was checked by scanning electron microscopy (SEM) equipped with energy-dispersive X-ray spectroscopy (EDS). In addition to the major elements C (94 wt%) and O (5 wt%), minor elements detected were S (0.4 wt%), as well as Na, Cl, Pb (0.2 wt%), and trace amounts of Si, Al, Fe (0.1 wt%). Thus, the O/(C + O) atomic ratio of 0.045 in LP is higher than the value of 0.03 found in shungite [3].

X-ray powder patterns were obtained with a D8 Brucker diffractometer using Cu Kα radiation (1.5406 Å). Samples were scanned from 10° to 90° 2θ, with a 0.0197° 2θ step size and a counting time of 1 s per step.

Raman and micro-Raman spectroscopy experiments were conducted using several setups with different excitation wavelengths and integration times ranging from 1 to 10 s. In this work, Horiba Jobin-Yvon and OceanOptics QEPro spectrometers were used. The former were equipped with objectives x50 or x100 and 900 gr/mm or 1800 gr/mm gratings and were operated with an Ar+ laser and semiconductor excitation sources at 473.13 nm, 514.5 nm, 532 nm, and 660 nm. The QEPro Peltier-cooled spectrometer (IEMN) was operated with a 785 nm laser focused via a fiber optics on the samples. The spot size and spectral resolution of the micro-Raman setups were ~1–2 μm/0.7 μm and 2 cm^{-1}/0.7 cm^{-1} while the laser power on the samples was comprised between 1.5 mW and 20 mW. The experiments were conducted on up to six different samples, with measurements repeated at various locations on the surface of each sample. A visual inspection was performed after each experiment to confirm that the laser spot caused no damage to the sample. The Raman spectra were calibrated using the 520.5 cm^{-1} Raman line of silicon.

The DFT calculations were performed using the Gaussian 16 program [11] at the B3LYP/6–311 G level of theory, and vibrations were analysed using the molecular modelling software Jmol. The theoretical Raman spectra were obtained with a graphical user interface [12].

3. Results and discussion

3.1. X-ray diffraction

For reference to the study below, the XRD patterns of graphite reveal at least four distinctive reflections (see Fig.2): (002), (010), (004), and (110) at 2θ = 26.4°, 42.5°, 54.6°, and 77.5°, respectively. The (002) and (004) peaks indicate the interlayer spacing and stacking of graphene sheets, with $d_{(002)}$ = 3.35 Å In contrast, the (010) and (110) peaks are associated with the in-plane spacing between carbon atoms and their arrangement within the graphene layers. The 2θ values of these graphite peaks are key indicators for the structural characterization of carbon-based materials.

The XRD powder pattern of Lopérec pyrobitumen (Fig. 2) reveals two prominent peaks characteristic of amorphous carbon. The main (002) peak is centered at 2θ = 24.9(1)°, corresponding to $d_{(002)}$ = 3.57(1) Å, with a full width at half maximum (FWHM), referred to as $\beta_{(002)}$ equal to 5.64° In contrast, shungite exhibits a small shift of this reflexion to a significantly higher 2θ value of 25.6(1)°, with smaller $d_{(002)}$ = 3.48(1) Å and a narrower $\beta_{(002)}$ = 3.6°, while its secondary (010) and (110) peaks centered at 2θ = 43.1° and 78.7° show similar positions found in pyrobitumen, i.e. 43.0° and 78.6°, respectively. The intensity of (010) peak in shungite and pyrobitumen is ~28 % and ~30 % of the main (002) peak, respectively. A very weak (004) peak at 2θ ≈ 54° observed in KS cannot be clearly resolved in LP. The extremely weak intensity of the (004) peak compared to the (002) peak suggests that Lopérec pyrobitumen is a non-graphitizing carbon [13].

The $d_{(002)}$ value for shungite agrees with those (3.47–3.52 Å) reported by Golubev et al. [13], whereas the $d_{(002)}$ for Lopérec pyrobitumen is significantly higher than the values typically observed in different poorly crystalline carbons [2]. The augmentation in $d_{(002)}$ follows the sequence graphite → shungite → pyrobitumen, reflecting the increase of structural disorder and an expansion of the average distance between graphene layers. Conversely, the $d_{(010)}$ and $d_{(110)}$ values of these two SK and LP amorphous carbons are slightly lower than those of graphite.

The characteristics of the main (002) peak of both materials can be analyzed following Wada et al. [14]. The apparent coherent length $L_{c(002)}$ (i.e., the crystallite thickness in Å), defined by the Scherrer equation, is given by $L_{c(002)} = 0.9\ \lambda_{CuK\alpha}/(\beta_{(002)}\cos\theta)$, where $\beta_{(002)}$ is expressed in radians. For Lopérec pyrobitumen, $L_{c(002)}$ is calculated to be 1.4 nm, compared to 2.0 nm for shungite. Finally, the values of graphitization degree for LP and KS are 6.9 and 13.1, respectively, by using the following relationship proposed by Tagiri [15]:

$$DG = [(d_{(002)} - 3.7)/\log(L_{c(002)}/1000)] \times 100 \quad (1)$$

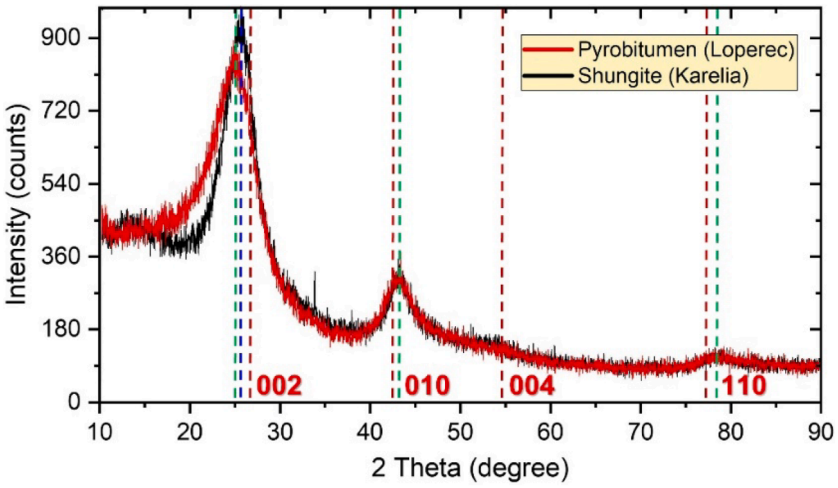

Fig. 2. XRD patterns of Loperec pyrobitumen (red) and shungite (black). Vertical doted lines: Positions of diffraction lines for: graphite (theoretical, red), Loperec pyrobitumen (green), and shungite (blue).

3.2. Raman spectroscopy

3.2.1. Raman features in graphene

The interpretation of the Raman spectra of Lopérec pyrobitumen and shungite is based on that of graphene and graphite. In *defect-free* planar graphene [16–18], the vibrational representation at the Γ point of the first Brillouin zone [BZ, $q = (0,0,0)$] is given by:

$$\Gamma_{vib} = A_{2u} + E_{1u} + B_{2g} + E_{2g} \quad (2)$$

In this representation, the three acoustic modes exhibit A_{2u} and E_{1u} symmetry, while the three optical modes are characterized by B_{2g} (Raman inactive) and E_{2g} (Raman active) symmetry. Among them, only the doubly degenerate E_{2g} mode contributes to the first-order Raman spectrum of graphene. This mode, associated with the sp^2 C—C stretching in the graphene honeycomb structure, gives rise to the G peak around 1590 cm^{-1}. Note that the position and shape of the G peak are signatures of changes in the crystalline structure, such as the presence of structural defects, charges, or strain.

The Raman spectrum of *defective* graphene exhibits an additional D peak at ~1350 cm^{-1}, originating from the breathing transverse optical (TO) mode of benzene rings activated at the K-point of the BZ through double resonant processes, enhancing its intensity [19,20]. This peak can be related to sp^3 structural defects or armchair edges for instance, with frequency depending on the excitation laser energy (E_L). Additionally, Raman spectra of sp^2 carbon materials such as graphene exhibit a prominent peak between 2500 and 2800 cm^{-1} that is known as the 2D band. This band originates from a second-order two-phonon process, causing its frequency to vary with E_L.

3.2.2. Comparison of Raman spectra of Karelian shungite and Lopérec pyrobitumen

Fig. 3 shows micrographs of the two carbonaceous compounds examined through Raman spectroscopy, captured using a binocular microscope. The samples can be described as brittle, black, shiny and lustrous chunks exhibiting distinct conchoidal fractures whose surfaces have a smooth, curved appearance, indicative of poorly defined macroscopic crystalline structures with dominant amorphous character.

The Raman spectra of LP and KS samples are compared in Fig. 4 with those of several carbon allotropes. The repeatability of the spectral quality was consistently high across different samples and spectrometers, confirming the excellent purity and homogeneity of the selected geomaterials. To the best of our knowledge, neither the Raman scattering of pyrobitumen, which has never been spectrally investigated, nor that of shungite, has been previously studied using these specific laser energies. These spectra, characterized by a high signal-to-noise ratio across the entire frequency range and an absence of photoluminescence, display features typical of disordered or poorly ordered carbon materials. Moreover, they reveal two well-defined regions, i.e. 1000–2000 cm^{-1} (first-order spectrum) and 2000–3200 cm^{-1} (second-order spectrum).

The LP and KS spectra shown in Figs. 4 and 5 exhibit a strong resemblance, each featuring a distinct peak at 1356–1359 cm^{-1} (D band) and another prominent peak around 1590 cm^{-1} (G band), along with a well-resolved second-order 2D spectrum. The intensity of the D band suggests a similar origin to that found in defective graphene. In the spectrum of pyrobitumen sample acquired at $\lambda_L = 473$ nm, the low-frequency region displays additional bands at 122, 139, 214, 276, 388, 476, 590, and 822 cm^{-1}. These bands are likely due to mineral micro-inclusions but do not appear to originate from pyrite. Moreover,

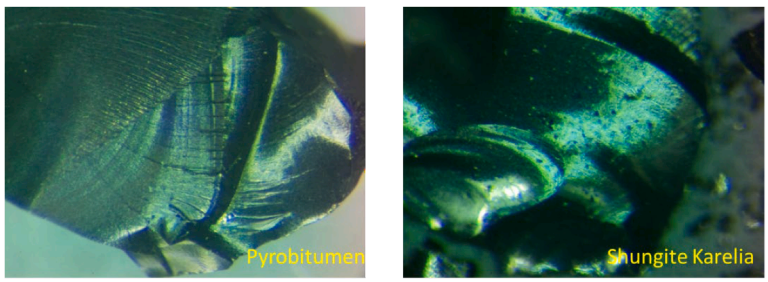

Fig. 3. Microphotographs of Lopérec pyrobitumen (left) and Karelian shungite (right) samples taken at same magnification. Field of view (width of the image): 2 mm.

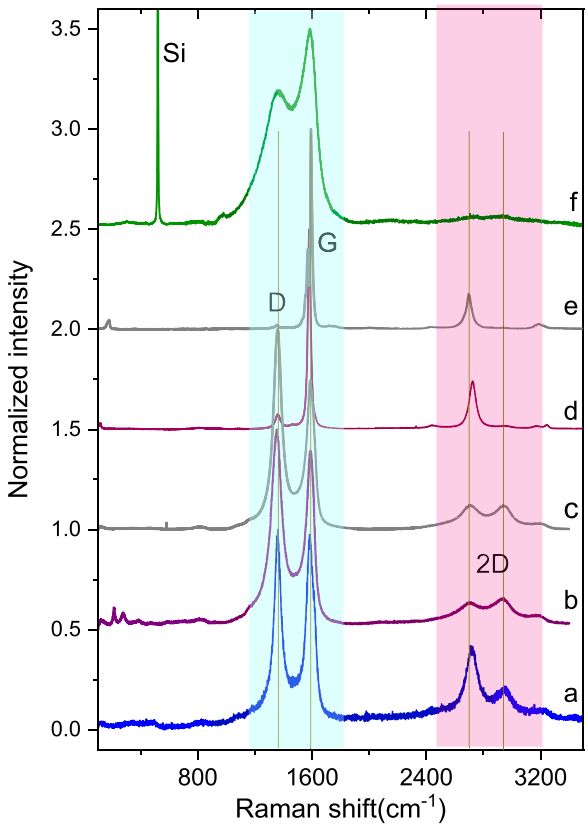

Fig. 4. Raman spectra of (a) multi-walled carbon nanotubes (MWNTs); (b) pyrobitumen from Lopérec; (c) shungite from Karelia; (d) pyrolytic graphite; (e) single-walled carbon nanotubes (SWNTs, NanoIntegris 96); and (f) an amorphous carbon layer on a Si wafer, obtained using 473.13 nm laser excitation on the IEMN spectrometer.

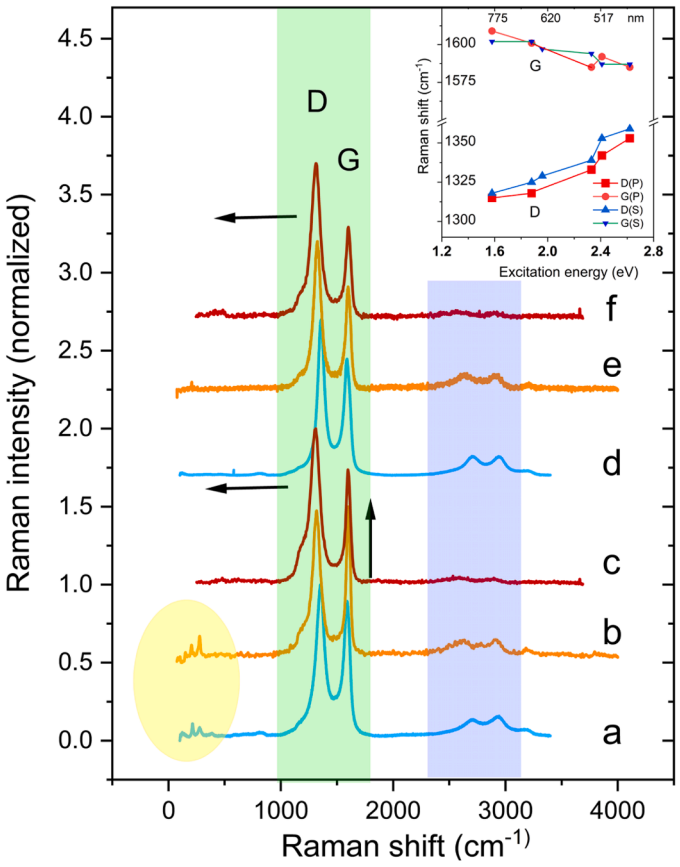

Fig. 5. Raman spectra of several samples of pyrobitumen from Lopérec (a-c) and shungite from Karelia (d-f) obtained with laser excitations at 473.13 nm (a, d), 660 nm (b,e) and 785 nm (c,f). The inset shows the variations of D1- and G-bands of LP and KS with excitation energy, from additional spectra obtained at λ_L = 514.5, 532 nm, 632.8 nm not shown here.

despite the presence of a line at 276 cm^{-1}, the Raman spectra lack the characteristic sharp peaks of natural fullerenes (489 and 1467 cm^{-1}), suggesting that fullerenes were not detected in our samples [21].

The KS and LP spectra obtained at 473 nm are consistent with previously published results for shungite and anthraxolite at other excitation wavelengths [13,22]. Although single-walled carbon nanotubes (SWNTs) and pyrolytic graphite exhibit weaker d-band intensities (Fig. 4e, d), it is noteworthy that the spectra of shungite and pyrobitumen (Fig. 4b, c) closely resemble those of multi-walled carbon nanotubes (MWNTs) under the same excitation conditions (Fig. 4a). Additionally, they do not display the features typical of *amorphous carbon*, which is characterized by very broad D and G bands in comparison (Fig. 4f). The D and G bands occur at the same frequencies in both KS and MWNTs (1357 and 1588 cm^{-1}), and the G band profiles are similar, with a shoulder around 1612 cm^{-1}. In MWNTs, the D and G bands have nearly equal intensities, whereas in KS, the G band is lower in intensity compared to the D band. Furthermore, in MWNTs, the first band of the 2D massif (at 2718 cm^{-1}) is relatively intense compared to the other components, in contrast to the 2D spectra of KS and LP. The strong similarity between the Raman spectra of MWNTs and shungite is a particularly interesting observation that aligns well with the concentric, onion-like structure observed in black slates and shungites through high-resolution transmission electronic microscopy (HRTEM) analysis, showing carbon walls reminiscent of MWNT structures (see Fig. 4B,C in Buseck [23]). The HRTEM studies of shungite are therefore fully consistent with the Raman spectra we present here for both geocarbons. Their spectra exhibit a profile, shape, and intensity that are strikingly similar to those of synthetic MWNTs, which naturally possess a multi-layered structure. As a result, it is clear that pyrobitumens also likely possess lamellar structures at the nanometer scale, inferred from this observed correspondence.

Still, the spectra of LP and KS recorded at λ_L = 660 nm and 785 nm (see Fig. 5) display several differences. In particular, the LP spectrum shows a more intense G line relative to the D line compared to the KS spectrum. Additionally, at the same wavelength of excitation and the same power density on the sample, we observe that the spectrum of KS is typically more intense than that of LP, in agreement with X-ray data which shows a higher graphitization for shungite.

In the second-order region, the two main peaks in shungite exhibit nearly equal intensities (Fig. 5c,d). Conversely, for Lopérec pyrobitumen, the second peak at 2932/2912 cm^{-1} is significantly more intense than the first peak at 2704/2623 cm^{-1} (Fig. 5a,b). This observation is consistent with the Raman spectra obtained at λ_L = 514.5 nm by Jehlička et al. for other carbonaceous materials and pyrobitumens [24]. This trend could also be indicative of a lower degree of structural order or graphitization.

An interesting observation for both LP and KS is the significant upshift of the D peak by 30 to 40 cm^{-1} as λ_L decreases (see inset of Fig. 5). In contrast, the G peak position in these compounds decreases at a much more gradual rate. As a result of the d-band downshift, the first and second bands in the second-order region show also a pronounced downshift at λ_L = 660 nm, whereas the weakest band of the 2D massif around 3100 cm^{-1} remains unchanged in both samples, regardless of the excitation wavelength. This behavior can be attributed to the dispersive nature of the D band, an A_{1g} mode, which varies with different laser energies (E_L), causing the 2D band composed of overtones and combinations of the D band to exhibit similar dispersion. This dispersion arises

because the energy of the A_{1g} mode includes a self-energy term related to electron-phonon interactions, which increases with higher E_L [25]. In contrast, the G band remains non-dispersive. Moreover, the G band of KS at 473 nm is shifted down by 5 cm^{-1} compared to that in the LP spectrum. This shift indicates that the C—C bonds within the graphene-like sheets of shungite are slightly less rigid than those in pyrobitumen, in agreement with X-ray diffraction data. In addition to the effects of graphenic interlayer interactions, this frequency shift may be attributed to internal strain within the shungite, leading to softer or more flexible C—C bonds. This phenomenon could also stem from the onion-like structure observed in these materials through HR-TEM analysis [23].

Fig. 6 highlights the correlation between the intensity ratio $R_1 = I_D/I_G$ and the full width at half maximum (FWHM) of non-differentiated D and G bands in the first-order spectra of KS and LP samples. The plot reveals two distinct regions: one below $R_1 = 1.1$ and another above $R_1 = 1.3$, which define spectral boundaries between LP and KS, respectively. This suggests that R_1 serves as a reliable indicator of the nature of the carbonaceous matter analyzed using Raman spectroscopy. The LP sample exhibits lower R_1 parameters and a higher FWHM for the D band recorded at $\lambda_L = 473$ nm, indicating a *reduced degree of structural order in this material* [26].

Chazhengina and Kovalevski [3] report for shungite a decrease in the intensity ratio $R_1 = I_D/I_G$ (global, non-differentiated G band) with temperature increase (i.e., by contact with a dolerite intrusion at relatively high temperature). According to Jehlička et al. [24], the least evolved types of carbonaceous matter formed at lower temperatures show an inverse trend, with G being greater than D. This observation is consistent with the study by Buseck and Beyssac (Fig. 5 in ref [20]), which shows that the G band intensity overcomes the D band from 700 to 420 °C, whereas the D band becomes more intense than the G band from 400 to 330 °C, and the G band intensity again exceeds the D band from 300 to 200 °C. Our Raman spectrum recorded at $\lambda_L = 660$ nm could reflect such transformations of Lopérec pyrobitumen at low temperatures in contrast to shungite.

3.2.3. *Deconvolution of Raman bands*

In general, narrower Raman bands in solids typically indicate higher crystallinity, with Lorentzian profiles representing well-ordered substances and Gaussian profiles characterizing highly disordered materials. For KS and LP samples explored in this work, the decomposition of the first-order (1000–2000 cm^{-1}) and second-order (2300–3300 cm^{-1}) scattering spectra can be achieved by superimposing Voigt functions that are often recommended for Raman line shapes of imperfect crystals or amorphous materials [27].

Several Raman studies of carbonaceous and graphenic materials [10, 13,17,24–28] have shown that the primary D and G broad bands observed in first-order Raman spectra result from the superposition of four to five sub-bands, namely D1, D2, D3, D4, D5, and G.

These sub-bands are listed in ascending frequency order, and are depicted in Golubev et al. (Fig. 3 in ref. [13]) and Ferralis *et al.* (Fig. 1 in ref. [28]). All the experimental Raman bands obtained for LP and KS spectra were fitted by using the Fityk program [29]. To accurately reproduce the Raman bands, Voigt function sub-bands were employed, including a D2 component at the edge of the G band. This methodology yields to satisfactory fits presented in Fig. 7 and Table 1. Specifically, the G massif of LP and KS first-order spectra comprises the main G line and the D2 sub-band, along with the D3 sub-band hidden at its low-frequency edge (Fig. 7a,c). In the high-frequency region (Fig. 7b,d), the bands represent combinations and overtones of these fundamental lines, which characterize the second-order Raman spectra.

In particular, at excitation $\lambda_L = 473$ nm, the overlapping bands in the first-order Raman spectrum are as follows: i) the most intense defect peak D1 is at ω_{D1} 1330–1360 cm^{-1}; ii) the peak D2 at ω_{D2} = 1600–1620 cm^{-1} which merges with the G line at ω_G = 1580–1600 cm^{-1} (with $\omega_G < \omega_{D2}$); iii) the band D3 at ω_{D3} = 1530–1540 cm^{-1} which contributes to the spectral weight between the two prominent D1 and G peaks; and iv) the D4 band appearing as a shoulder on the low-frequency edge of D1 at ω_{D4} = 1160–1200 cm^{-1}. In line with the methodology of Ref. 28, a weak D5 component at 1271 cm^{-1} was also included in the LP spectrum. This component is positioned close to the D4 band at 1171 cm^{-1}. This additional D5 component is essential for explaining the enhanced spectral intensity observed in the LP spectrum. It manifests as a discernible shoulder at the edge of the D1 band, in contrast to the smoother D1 profile in the KS spectrum. In turn, the D5 and the D3 bands are completely obscured by the D1 and G/D2 bands. Their presence is substantiated by (i) the necessity to include them in any fitting procedure of the Raman profiles obtained at λ_L = 473 nm, and (ii) the assignment of the 2D components. The D3 sub-band contributes mainly

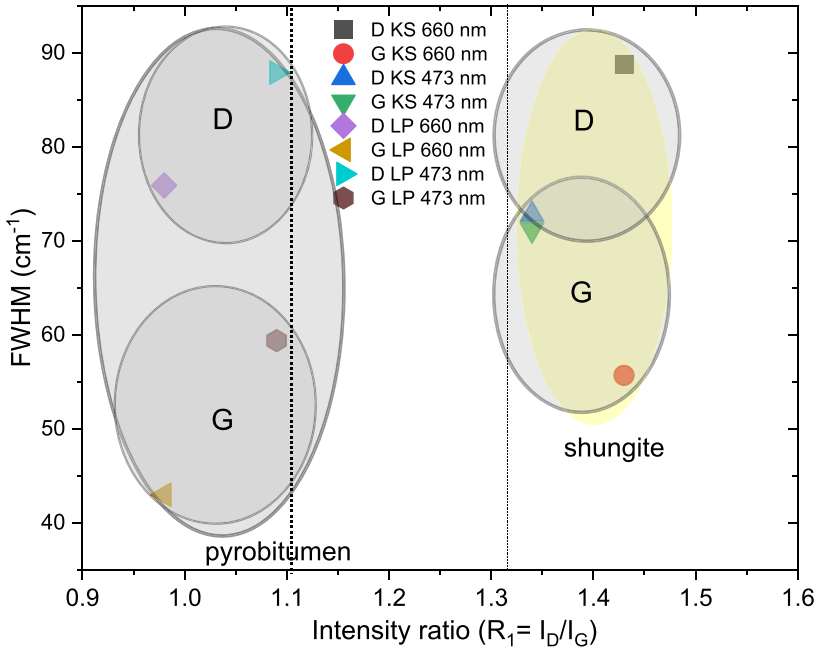

Fig. 6. Comparison of ordering in Karelian shungite and Lopérec pyrobitumen from Raman spectral intensities and FWHM of non-differentiated D and G bands, for the excitations 473 and 660 nm.

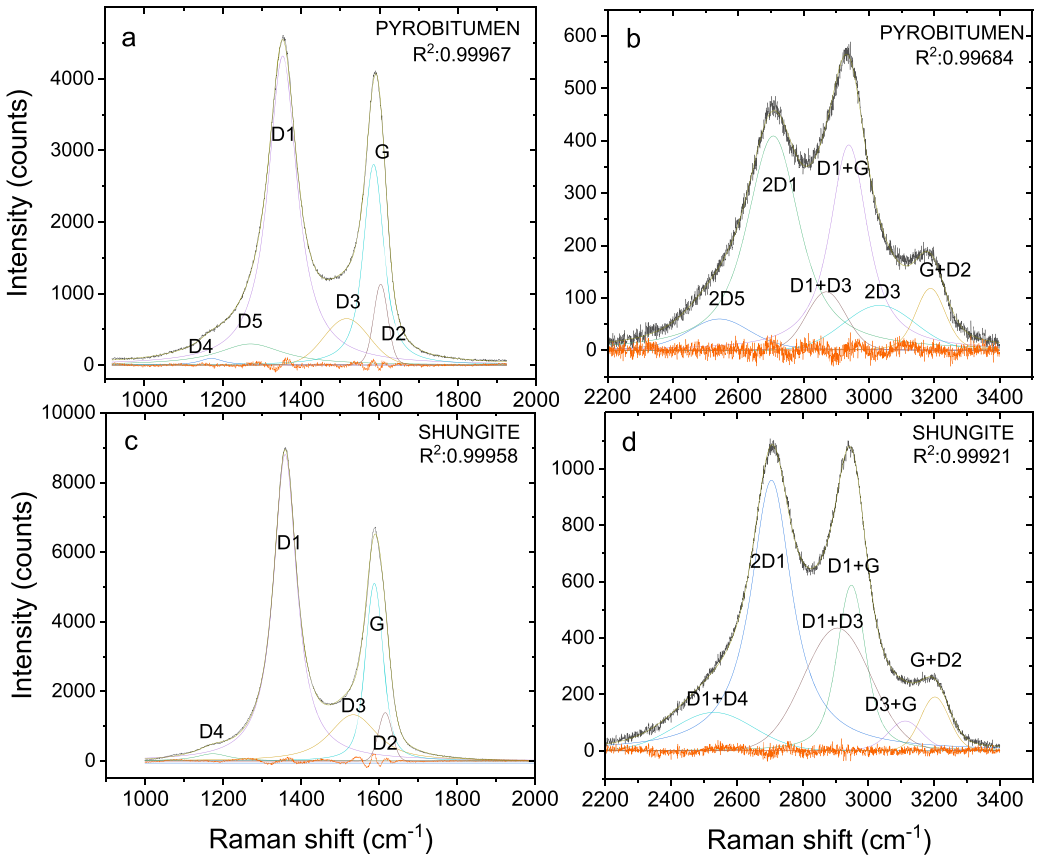

Fig. 7. Voigt fits with residuals of the first-order (a, c) (D/G region) and second-order (b, d) Raman spectra for pyrobitumen from Lopérec and shungite from Karelia (2D region). λ_L = 473 nm. The coefficients of determination (R^2 close to 1) indicate a good fit between the model and the experimental data.

Table 1
Raman components of the D and G massifs (in cm^{-1}) obtained with Voigt fits and estimates of graphitic layer size and tortuosity in nm using the relations of Cançado et al. [35] (*) for E_L =2.62 eV (473 nm), Tuinstra-Koenig [16](†), Larouche et al. [37] (‡), and Golubev et al. [13] (£). G means G component.

	D4	D5	D1	D3	G	D2	L_a	L_t
Karelian shungite	1174	–	1359	1533	1587	1615	8.2*	11.3*
							3†	4.1‡
							5.1†	6.2†
Lopérec pyrobitumen	1171	1271	1353	1516	1585	1603	6.7*	9.2*
							2.5†	3.3‡
							4.9£	4.6£
Method of this work (*)	$A_D = A_{D4}+A_{D5}+A_{D1}$		A_G (global) $=A_{D3}+A_G+A_{D2}$					
Method of Golubev et al. (£)	$L_a \propto A_G/A_{D1}$		$L_t \propto A_{2D1}/A_{D1}$					

to the higher spectral weight between the global D and G bands in the two samples, whereas the D2 component contributes more significantly to the G band intensity in pyrobitumen.

The second-order spectrum of KS and LP at higher frequencies, i.e., the 2D region in Fig. 7b,d, shows some similarity to that of graphite and graphene oxide. It is characterized by weaker and broader lines with sub-bands that are more difficult to separate. The first shoulder, observed around 2380–2550 cm^{-1}, can be identified as the D1+D4 combination band or possibly the 2D5 overtone. The broader and more intense bands near 2680 cm^{-1} and 2950 cm^{-1} are attributed to the 2D1 and the $G + D1$ overtones, respectively, as evidenced by the downshift of these bands with decreasing excitation energy. The weakest feature at ~3190 cm^{-1} corresponds to the $G + D2$ combination. To accurately fit the spectral envelope, hidden bands centered at ~2870 cm^{-1} and ~2930 cm^{-1} must be included, which could be attributed to the D3+D1 combination. However, this assignment may vary depending on the specific sample, i.e., shungite or pyrobitumen, and the excitation wavelength used to record the Raman spectra.

In ref. [30] (Dychalska), the authors compared Raman shifts for various forms of carbon, including *trans-polyacetylene*. In this context, the weak D4/D5 bands observed around 1170–1270 cm^{-1} in the current geomaterials are unlikely to originate from polyene segments with alternating single C–C and double C = C bonds laying at the grain boundaries of the materials. The shortest segments in this polymer, when investigated using UV or blue laser excitations, typically exhibit a prominent band around 1130 cm^{-1} [30,31], as confirmed theoretically by Mulazzi's segment distribution model [32]. Furthermore there is no C = C band between 1400 and 1500 cm^{-1} in the spectra. Additionally, the entire Raman spectra of KS and LP exhibit characteristics akin to those observed for disordered or *degraded polyparaphenylene* (PPP) studied by Marucci et al. [33], which show first-order peaks around 1200, 1320, and 1600 cm^{-1}, and second-order peaks between 2800 and 3200 cm^{-1}. More notably, they also closely resemble the spectra of shocked graphite, *graphene oxide* and as seen above (Fig. 4a) to those of *multi-walled carbon nanotubes* [20,34]. Therefore, it is reasonable to attribute the prominent Raman lines observed in LP and KS to vibrations of

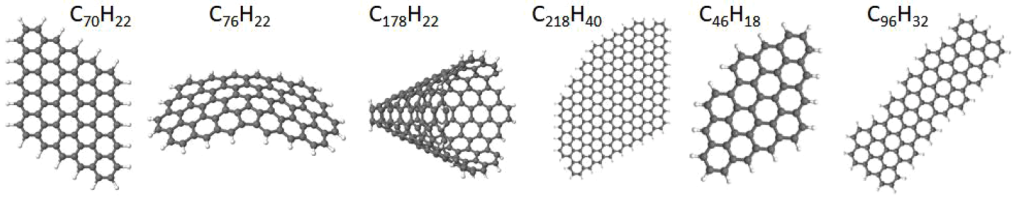

Fig. 8. Examples of hydrogen-passivated carbon nanostructures calculated using DFT in this work.

benzenoid structures within small graphene flakes. In these carbonaceous natural materials, the D1 Raman band can be ascribed to the defect modes in graphenic structures, as suggested by the d-band observed in defective graphene [20] and further supported by DFT calculations (see below). The intensity of this band reflects significant structural disorder.

3.2.4. Size and tortuosity of graphitic domains

To explore the nanostructure of the present samples, specific ratios of the relative intensities of the main Raman bands can be used to estimate roughly the sizes of different microcrystalline domains within the disordered matrix.

To this purpose, the relationship established by Cançado et al. [35] was utilized, which connects a Raman intensity ratio of the D to G bands with the average layer size L_a of graphitic domains, depending on the fourth power of the laser energy (E_L) used in each Raman experiment:

$$L_a(nm) = \frac{560}{E_L^4} \times \frac{I_G}{I_D} = a \times R \quad (3)$$

The proportionality constants a are 12.026 nm, 16.606 nm and 45.539 nm for E_L =2.62 eV (473.13 nm), 2.41 eV (514.5 nm) and 1.88 eV (660 nm), respectively. In the case of excitation at 514.5 nm, the a value is nearly four times higher than the value of $a = 4.4$ previously reported by Tuinstra and Koenig [16] and Knight et al. [36]. The tortuosity L_t of the graphene-like flakes in the samples can be defined by evaluating the intensity ratio of the 2D band to the D band as suggested by Larouche et al. [37]:

$$L_t = 2a\frac{A_{2D}}{A_D} \quad (4)$$

These authors estimate the proportionality constant to be twice the value of that of the L_a parameter. The L_t parameter measures the size of a curved graphene flake composed of small planar regions of length L_a. To estimate these parameters, the areas of the global non-differentiated D, G, and 2D bands of LP and KS (i.e., the sum of their components) were considered, as described in Refs. 16,30, 37. Specifically, the entire 2D massif was integrated between 2400 and 3400 cm^{-1} to obtain the value of A_{2D}. Meanwhile, A_D was determined by summing the areas of D4 (D5), and D1, while A_G was obtained by adding the areas of D3, G and D2. Table 1 summarizes the Raman components obtained from the fits, along with the values of L_a and L_t calculated using either $a = 4.4$ or Cançado's formula.

The observed sizes match the longitudinal dimensions of graphite layer fringes reported in HRTEM studies of Karelian shungite by Buseck and Beyssac [23], with L_a or L_t ranging from 5 to 10 nm, compared to 2–5 nm in more disordered black slate. These results are also consistent with the approximately 3 nm crystallite sizes reported by Golubev et al. [13] in anthraxolites and by Sheka and Rozhkova [38] in shungite. Additionally, when using the component ratios A_G/A_{D1} and A_{2D1}/A_{D1} as suggested in Ref. 13, the L_a or L_t values for shungite remains greater than those for pyrobitumen. Regardless of the method employed, these evaluations indicate that LP material exhibits degraded ordering and reduced graphitization compared to KS. This suggests a less extensive and less coherent crystalline structure, in line with the estimates derived from X-ray data.

3.2.5. DFT simulation and identification of Raman components

To complement the Raman study, *in-vacuo* density functional theory (DFT) calculations were performed on hydrogen-passivated graphene flakes and nanocarbons of varying dimensions. The flake sizes were selected to balance computational efficiency and accuracy. Hydrogen atoms were positioned in planar configuration at the nanoflake's edges to maintain the neutrality and stability of the structures. Calculations were undertaken on $C_{46}H_{18}$ (1.56 nm × 0.87 nm), $C_{70}H_{22}$ (1.26 nm × 2.01 nm), $C_{76}H_{22}$ (curved flake, 1.90 nm x 0.92 nm), $C_{96}H_{32}$ (2.68 nm × 0.87 nm), $C_{218}H_{40}$ (2.09 nm × 3.69 nm), $C_{84}H_{20}$ (bent flake, ~1.29 nm × 1.23 nm), $C_{84}H_{24}$ (curved flake), and $C_{47}H_{17}$ (1.46 nm x 0.70 nm). In addition we calculated a H-passivated nanocone $C_{178}H_{22}$ (1.38 nm × 1.79 nm). Except $C_{96}H_{32}$ which is a nanoribbon with 2 long armchair edges, the nanoflake edges are dominantly zigzag, with armchair "corners" (Fig.8).

The primary goal of these DFT calculations was to identify the graphene flake shapes that produce theoretical Raman spectra most closely matching the experimental spectra recorded for shungite and pyrobitumen samples at different excitation wavelengths. In this way, the most

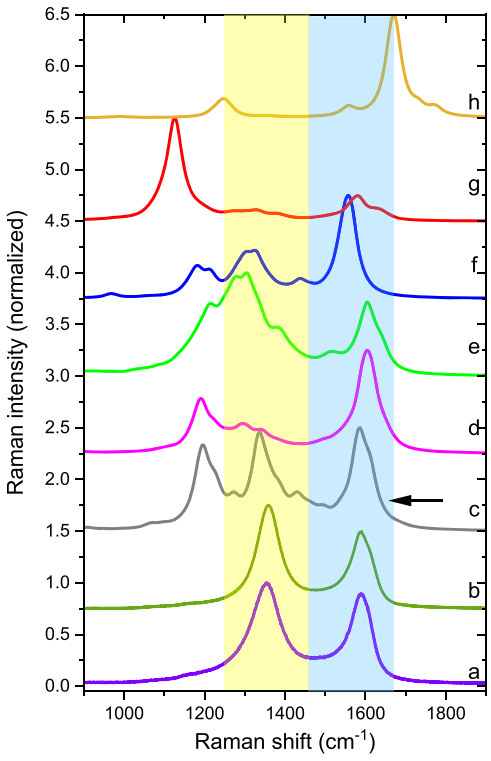

Fig. 9. Comparison between the experimental first-order Raman spectra of: (a) pyrobitumen, (b) shungite for λ_L = 473 nm and the theoretical Raman spectra obtained for H-passivated carbon nanostructures; (c) $C_{70}H_{22}$; (d) $C_{178}H_{22}$ nanocone; (e) $C_{218}H_{40}$ cone sheet; (f) $C_{46}H_{18}$; (g) $C_{96}H_{32}$ nanoribbon; (h) DWNT crowns ($C_{92}H_{46}$, 1.26/0.55 nm, spacing 0.35 nm, Hartree-Fock level). Scaling factor: 0.962. For DFT and HF spectra, the bands are convoluted using Lorentzian profiles with a FWHM of 20 cm^{-1}. Colored stripes highlight the regions of D and G bands.

Table 2
Assignment of the D and G vibrational components in shungite and pyrobitumen based on DFT calculations of $C_{70}H_{22}$ frequencies (in cm^{-1}). ν, β, denote stretching, and in plane bending, respectively.

Component	Experimental Frequencies	Theoretical assignment
D4	1195	β(CH); antisymmetric ν(CC) edge mode
D5	1272	β(CH); symmetric ν(CC) edge mode
D1	1337	β(CH); antisymmetric ν(CC)
D1 shoulder	1380	benzene ring breathing
G	1585	β(CH); long axis symmetric ν(CC)
D2	1608	β(CH); symmetric ν(CC)

appropriate spectra could reveal the origin of the D and G Raman band components in greater detail than previously described empirically. Theoretical spectra compared to experimental ones are shown in Fig.9. Among all the Raman simulations, the best agreement is found for $C_{70}H_{22}$, and $C_{76}H_{22}$ (Fig. 9c,d), which are analogous to "planar" graphene quantum dots (GQD). The former structure has almost exact match for D and G band frequencies. It exhibits D_{2h} symmetry and features both zigzag and armchair edges, with an average C—C bond length of 0.143 nm and C—H bond lengths of 0.11 nm. Although the Lopérec pyrobitumen samples contains 5 % oxygen, our simulation excluded oxygen atoms from the model. In this context, it is worth noting also that the nanostructure of shungite can be modelled as a framework composed of reduced graphene oxide (rGO) nanosheets [38,39]. The DFT calculations conducted in the present work provide, for the first time to our knowledge, a clear preliminary vibrational assignment of the D1, D2, D3, D4, D5, and G Raman sub-bands observed in carbonaceous materials (Table 2).

The close match between the experimental and calculated D and G bands, along with the sizes inferred from the Raman band ratios, suggests that the sharp D and G experimental Raman bands observed in natural carbonaceous materials such as shungite and pyrobitumen likely originate from highly disordered carbon nanostructures, specifically graphene quantum dots [38,40]. These structures exhibit a range of sizes, from 1 to 2 nm as determined by DFT simulations, to 7 nm and 11 nm as inferred from Raman data.

3.3. Pyrobitumen formation

Loperec pyrobitumen constitutes a well-defined, homogeneous sp^2 disordered carbon. Relatively to shungite, its lower density and its characteristics determined from X-ray and Raman studies indicate a higher disorder, i.e., a lower graphitization degree. In such non-graphitizable carbons, ordering is directly related to increasing temperature. This irreversible process enables the determination of the maximum temperature reached by carbon-containing rocks, as illustrated by Buseck and Beyssac in their study on the evolution of the Raman spectrum with metamorphic peak temperature [23].

In metamorphic process of sedimentary rocks, the degree of graphitization of carbonaceous material can be checked through X-ray diffraction by the position of $d_{(002)}$ peak and its FWHM (2θ) [41,42]. A similar approach has been developed based on Raman spectroscopy [23,43].

Wada et al. [14] established two regression lines correlating temperature T (in °C) and graphitization degree DG in metamorphic sequences:

$$T = (3.8 \times DG) + 200(\text{limestones}) \quad (5)$$

$$T = (3.2 \times DG) + 280(\text{pelitic rocks}) \quad (6)$$

Using DG values derived from the X-ray study, Eq. (5) yields temperatures of 226 °C for Loperec pyrobitumen and 250 °C for shungite, while Eq. (6) gives 302 °C and 322 °C, respectively. The latter value is more consistent with the known formation temperature of shungite (T ~ 350 °C) [3]. One can thus propose T ~ 300 °C for the formation of pyrobitumen at Loperec.

This is consistent with previous studies on metamorphic rocks [23,43]:

(i) The shoulder attributed to D4 at ~1160–1200 cm^{-1} in the graphitic carbon of these geomaterials (or D5 in our pyrobitumen sample) becomes increasingly pronounced in the Raman spectrum as the temperature decreases from 360 °C to 200 °C;
(ii) The inversion of the G/D intensity ratio (Fig. 5 in ref. [23]) occurs between 330 °C ($G/D < 1$ → shungite type) and 300 °C ($G/D > 1$ → Loperec type).

At Loperec, pyrobitumen appears as the final residue of the thermal degradation (chemical alteration) of a local source of hydrocarbons, probably from the surrounding black shales. Taking into account the mineralogy of the ore vein, a geochemical process controlling its formation can be proposed according to redox process between (i) a local source of mobile hydrocarbon (gas or oil), and Fe-rich minerals, and (ii) an oxidizing hydrothermal solution. The deposition of iron carbonate implies a CO_2-rich solution. Precipitation of the pyrobitumen results from the oxidation of the mobile hydrocarbon. Such a hydrothermal ore vein with a strong correlation between gold and carbon matter deposition is similar to carbon-rich gold-bearing quartz veins of Erickson gold mine (British Columbia, Canada) described by Mastalerz et al. [44,45]. Nevertheless, these authors consider carbon veins as the result of the reduction of CO_2 (and not organic matter) from adjacent sediments by H_2.

The Saint-Aubin-des-Châteaux quarry (West of the Armorican Massif) is another interesting example of interaction between a local hydrocarbon source (carbon-rich oolitic ironstone) and an oxidizing hydrothermal solution [46]. Sulfidation of the ironstone induced the formation of massive pyritized lenticular bodies. Here the ironstone siderite was dissolved by an acidic solution, and the reduction of the sulfate ions in solution by organic matter furnished S^{2-}, whose combination with Fe^{2+} from dissolved siderite gave pyrite deposition [47]. Contrary to Lopérec geochemical process, here primitive solid organic matter was strongly oxidized, and dissolved as CO_2, with only rare lamellar graphite crystals as solid by-product.

4. Conclusion

Two important classes of geocarbons, shungite and pyrobitumen, were analyzed using Raman spectroscopy and X-ray diffraction, with their properties compared to those of synthetic carbon allotropes. These experiments, supported by DFT calculations, allowed for nanoscale characterization of the materials. The Raman spectra exhibited a remarkable empirical similarity to those of multi-walled carbon nanotubes, suggesting the presence of multi-layered nanostructures within these geomaterials. However, despite their comparable spectral features, X-ray diffraction patterns and Raman analyses revealed differences in the average size of the graphenic nanostructures between the two carbonaceous materials.

Overall, pyrobitumen from Lopérec is a more disordered material compared to Karelian shungite, reflecting its lower degree of graphitization. Notably, the experimental Raman spectra of both geomaterials closely match those of theoretically calculated graphene quantum dots measuring 1–2 nm in size, enabling a more detailed vibrational assignment of the D and G bands (D1-D5). Furthermore, precise description of the relative intensities of the D and G bands support the conclusion that the Lopérec gold vein deposit represents a unique French occurrence of pyrobitumen, formed by a hydrothermal process at approximately 300 °C through the oxidation of a local hydrocarbon source.

Due to its relative abundance at the site and the high purity demonstrated by Raman spectra, Lopérec pyrobitumen emerges as a promising material for further analytical investigations, including carbon isotope analysis, infrared spectroscopy, and chromatography-mass

spectrometry. Additionally, the study of fluid inclusions in the associated quartz would enable precise determination of the temperature and chemical composition of the hydrothermal solution involved in its formation.

CRediT authorship contribution statement

Eric Faulques: Conceptualization, Data curation, Formal analysis, Funding acquisition, Investigation, Methodology, Supervision, Validation, Visualization, Writing – original draft, Writing – review & editing. **Nataliya Kalashnyk:** Supervision, Validation, Visualization, Writing – original draft, Writing – review & editing. **Yves Lulzac:** Investigation. **Yves Moëlo:** Conceptualization, Data curation, Formal analysis, Investigation, Methodology, Supervision, Validation, Visualization, Writing – original draft, Writing – review & editing.

Declaration of competing interest

The authors declare that they have no known competing financial interests or personal relationships that could have appeared to influence the work reported in this paper.

The author is an Editorial Board Member/Editor-in-Chief/Associate Editor/Guest Editor for *[Nanomaterials]* and was not involved in the editorial review or the decision to publish this article.

Acknowledgements

This study was supported by the IEMN PCMP platform of the French Technological Network RENATECH. DFT calculations were performed on Centre de Calcul Intensif des Pays de la Loire (CCIPL). SEM analyses were performed by N. Stéphant (IMN). We thank J.F. Marion (Douarnenez, Finistère dpt., France), for providing us the main part of Lopérec samples.

Data availability

Data will be made available on request.

References

[1] R.J. Hwang, S.C. Teerman, R.M. Carlson, Geochemical comparison of reservoir solid bitumens with diverse origins, Org. Geochem. 29 (1998) 505–517, https://doi.org/10.1016/S0146-6380(98)00078-3.
[2] V.V. Kovalevski, P.R. Buseck, J.M. Cowley, Comparison of carbon in shungite rocks to other natural carbons: An X-ray and TEM study, Carbon. N. Y. 39 (2001) 243–256, https://doi.org/10.1016/S0008-6223(00)00120-2.
[3] S.Y. Chazhengina, V.V. Kovalevski, Structural characteristics of shungite carbon subjected to contact metamorphism overprinted by greenschist-facies regional metamorphism, Eur. J. Min. 25 (2013) 835–843, https://doi.org/10.1127/0935-1221/2013/0025-2327.
[4] V.I. Berezkin, A soot model for the genesis of Karelian shungites, Rus. Geol. Geoph. 46 (2005) 1093–1101.
[5] V. Bouchot, J.P. Milési, J.L. Lescuyer, P. Ledru, Les minéralisations aurifères de la France dans leur cadre géologique autour de 300 Ma, Chron. Rech. Min. 528 (1997) 13.
[6] E. Marcoux, Mines Et Ressources Minérales En Armorique (2017) 466.
[7] E. Marcoux, Etude Minéralogique D'échantillons De Lopérec, Unpub. BRGM report 92/SGN/GEO/PMG/017/em/cm, Orléans, 1992, p. 14.
[8] V. Kovalevski, V. Shchiptsov, Shungites and their industrial potential, in: Proc. 14th International Congress for Applied Mineralogy (ICAM2019), Sergey Glagolev Ed, Springer Proceedings in Earth and Environmental Sciences, Springer Open, 2019, pp. 201–204, https://doi.org/10.1007/978-3-030-22974-0_47.
[9] W. Hanneman, Three secret of gemstone identification, Gems and Minerals (1972) 26–29. January vol.
[10] Y.A. Golubev, I.V. Antonets, Electrophysical properties and structure of natural disordered sp2 carbon, Nanomaterials 12 (2022) 3797–3821, https://doi.org/10.3390/nano12213797.
[11] M.J. Frisch, et al., Gaussian 16, Revision A.03, Gaussian, Inc., Wallingford CT, 2016.
[12] A.R. Allouche, Gabedit - A graphical user interface for computational chemistry softwares, J. Comp. Chem. 32 (2011) 174, https://doi.org/10.1002/jcc.21600.
[13] Y.A. Golubev, S.I. Isaenko, A.S. Prikhodko, N.I. Borgardt, E.I. Suvorova, Raman spectroscopic study of natural nanostructured carbon materials: shungite vs. anthraxolite, Eur. J. Mineral. 28 (2016) 545–554, https://doi.org/10.1127/ejm/2016/0028-2537.
[14] H. Wada, T. Tomita, K. Matsuura, K. Iuchi, M. Ito, Graphitization of carbonaceous matter during metamorphism with references to carbonate and pelitic rocks of contact and regional metamorphisms, Contrib. Mineral. Petrol. 118 (1994) 217–228, https://doi.org/10.1007/BF00306643.
[15] M. Tagiri, A measurement of the graphitizing-degree by the X-ray powder diffractometer, J. Jpn. Assoc. Mineral. Petrol. Econ. Geol. 76 (1981) 345–352, https://doi.org/10.2465/ganko1941.76.345.
[16] F. Tuinstra, J.L. Koenig, Raman Spectrum of Graphite, J. Chem. Phys. 33 (1970) 1126–1130, https://doi.org/10.1063/1.1674108.
[17] A.C. Ferrari, D.M. Basko, Raman spectroscopy as a versatile tool for studying the properties of graphene, Nature Nanotech 8 (2013) 235–246, https://doi.org/10.1038/nnano.2013.46.
[18] A.K. Ott, in: T. Chakraborty (Ed.), Raman spectroscopy of graphene and related materials. Encyclopedia of Condensed Matter Physics, 2nd ed., 2024, pp. 233–247.
[19] S.S. Nanda, M.J. Kim, K.S. Yeom, A. Seong Soo, S.S.A. An, H. Ju, D.K. Dong Kee Yi, Raman spectrum of graphene with its versatile future perspectives, Trends in Analytical Chemistry 80 (2016) 125–131, https://doi.org/10.1016/j.trac.2016.02.024.
[20] A.C. Sparavigna, Graphene, Graphene Oxide and Carbon Nanotubes in Raman Spectroscopy. Intern, J. Sci. 13 (2024) 1–26, https://doi.org/10.18483/ijSci.2773, and references therein.
[21] B.J. Saikia, G. Parthasarathy, B.K. Saikia, R.R. Borah, Occurrence of natural fullerene C60 from the iridium-rich Cretaceous-Paleogene (K-Pg) boundary layers of the Um-Sohryngkew riversection, Meghalaya, India, Carbon Trends 13 (2023) 100309, https://doi.org/10.1016/j.cartre.2023.100309.
[22] S.Y. Chazhengina, V.V. Kovalevski, Raman spectroscopy of weathered shungites, J. Raman Spectrosc. 48 (2017) 1590–1596, https://doi.org/10.1002/jrs.5188.
[23] P.R. Buseck, O. Beyssac, From organic matter to graphite: Graphitization, Elements 10 (2014) 421, https://doi.org/10.2113/gselements.10.6.421.
[24] J. Jehlička, O. Urban, J. Pokorny, Raman spectroscopy of carbon and solid bitumens in sedimentary and metamorphic rocks, Spectr. Acta Part A 59 (2003) 2341, https://doi.org/10.1016/S1386-1425(03)00077-5. -235.
[25] K-i Sasaki, Y. Tokura, T. Sogawa, The Origin of Raman D Band: Bonding and Antibonding Orbitals in Graphene, Crystals. (Basel) 3 (2013) 120–140, https://doi.org/10.3390/cryst3010120.
[26] S.Y. Chazhengina, A.V. Stepanova, V.V. Ustinova, S.A. Svetov, Amorphous carbonaceous material in Paleoproterozoic pillow lavas (Onega Basin, NW Russia): Origin, source and migration, Lithos. 460-461 (2023) 107373, https://doi.org/10.1016/j.lithos.2023.107373.
[27] T. Sundius, Computer fitting of Voigt profiles to Raman lines, J. Raman Spectr. 1 (1973) 471–488, https://doi.org/10.1002/jrs.1250010506.
[28] N. Ferralis, E.D. Matys, A.H. Knoll, C. Hallmann, R.E. Summons, Rapid, direct and non-destructive assessment of fossil organic matter via micro-Raman spectroscopy, Carbon. N. Y. 108 (2016) 440–449, https://doi.org/10.1016/j.carbon.2016.07.039.
[29] M. Wojdyr, Fityk: a general-purpose peak fitting program, J. Appl. Cryst. 43 (2010) 1126–1128, https://doi.org/10.1107/S0021889810030499.
[30] A. Dychalska, P. Popielarski, W. Frankow, K. Fabisiak, K. Paprocki, M. Szybowicz, Study of CVD diamond layers with amorphous carbon admixture by Raman scattering spectroscopy, Materials Science-Poland (2015), https://doi.org/10.1515/msp-2015-0067.
[31] S. Lefrant, E. Faulques, S. Krichene, G. Sagon, Raman Study of trans-polyacetylene and polyparaphenylene with excitation in the U.V. range, Polymer Commun 24 (1983) 361–363.
[32] E. Faulques, E. Rzepka, S. Lefrant, E. Mulazzi, G.P. Brivio, G. Leising, Polarized resonant Raman spectra of fully oriented trans-polyacetylene: Experiments and theory, Phys. Rev. B 33 (1986) 8622–8628, https://doi.org/10.1103/PhysRevB.33.8622.
[33] A. Marucci, M.A. Pimenta, S.D.M. Brown, M.J. Matthews, M.S. Dresselhaus, M. Endo, Study of the overtones and combination bands in the Raman spectra of polyparaphenylene-based carbons, J. Mater. Res. 14 (1999) 3447–3454, https://doi.org/10.1557/JMR.1999.0466.
[34] M. Wierzbicki, S. Jaworski, E. Sawosz, A. Jung, G. Gielerak, J. Biernat, et al., Graphene oxide-based nanocomposites decorated with silver nanoparticles as an antibacterial agent, Nanoscale Res. Lett. 13 (2018) 116, https://doi.org/10.1186/s11671-018-2533-2.
[35] L.G. Cançado, K. Takai, T. Enoki, M. Endo, Y.A. Kim, H. Mizusaki, et al., General equation for the determination of the crystallite size La of nanographite by Raman spectroscopy, Appl. Phys. Lett. 98 (2006) 163106, https://doi.org/10.1063/1.2196057. -1-3.
[36] D.S. Knight, W.B. White, Characterization of diamond films by Raman spectroscopy, J. Mater. Res. 4 (1989) 385–393, https://doi.org/10.1557/JMR.1989.0385.
[37] N. Larouche, B.L. Stansfield, Classifying nanostructured carbons using graphitic indices derived from Raman spectra, Carbon. N. Y. 48 (2010) 620–629, https://doi.org/10.1016/j.carbon.2011.06.033.
[38] E.F. Sheka, N.N. Rozhkova, Shungite as the natural pantry of reduced graphene oxide, Int. J. Smart Nano Mater. 5 (2014) 1–16, https://doi.org/10.1080/19475411.2014.885913.
[39] E.F. Sheka, I. Natkaniec, N.N. Rozhkova, K. Holderna-Natkaniec, Neutron scattering study of reduced graphene oxide of natural origin, JETP. Lett. 99 (2014) 754–759, https://doi.org/10.7868/S0370274X14110083.

[40] B.S. Razbirin, N.N. Rozhkova, E.F. Sheka, D.K. Nelson, A.N. Starukhin, Fractals of graphene quantum dots in photoluminescence of shungite, J. Exp. Theor. Phys. 118 (2014) 735–746, https://doi.org/10.1134/S1063776114050161.
[41] T. Itaya, Carbonaceous material in pelitic schists of the Sanbagawa metamorphic belt in central Shikoku, Japan, Lithos. 14 (1981) 215–224, https://doi.org/10.1016/0024-4937(81)90043-8.
[42] G.F Wang, Carbonaceous material in the Ryoke metamorphic rocks, Kinki district, Japan, Lithos. 22 (1989) 305–316, https://doi.org/10.1016/0024-4937(89)90032-7.
[43] O. Beyssac, B. Goffé, C. Chopin, J.N. Rouzaud, Raman spectra of carbonaceous material in metasediments: A new geothermometer, J. Metamorphic Geol. 20 (2002) 859, https://doi.org/10.1046/j.1525-1314.2002.00408.x.
[44] M. Mastalerz, R.M. Bustin, A.J. Sinclair, B.A. Stankiewicz, Carbon-rich material in the Erickson hydrothermal system, Northern British Columbia, Canada: Origin and formation mechanisms, Econ. Geol. 90 (1995) 938–947, https://doi.org/10.2113/gsecongeo.90.4.938.
[45] M. Mastalerz, R.M. Bustin, A.J. Sinclair, B.A. Stankiewicz, M.L. Thomson, 16. Implications of hydrocarbons in gold-bearing epithermal systems: Selected examples from the Canadian Cordillera. In Organic matter and mineralization: Thermal alteration, hydrocarbon generation and role in metallogenesis. Glikson & Mastalerz edit, Springer Science+Business Media Dordrecht (2000) 359–377, https://doi.org/10.1007/978-94-015-9474-5_17.
[46] E. Gloaguen, Y. Branquet, P. Boulvais, Y. Moëlo, J.J. Chauvel, P.J. Chiappero, E. Marcoux, Palaeozoic ironstone of the French Armorican Massif: a chemical and structural trap for orogenic base metal-As-Sb-Au mineralization during Hercynian strike-slip deformation, Miner. Deposita 42 (2007) 399–422, https://doi.org/10.1007/s00126-006-0120-4.
[47] Y. Moëlo, E. Fritsch, E. Gloaguen, O. Rouer, Polygenic chamosite from a hydrothermalized oolitic ironstone (Saint-Aubin-des-Châteaux, Armorican Massif, France): crystal chemistry, visible–near-infrared spectroscopy (red variety) and geochemical significance, Clay. Miner. 55 (2020) 83–95, https://doi.org/10.1180/clm.2020.13.